JOURNAL OF GEOPHYSICAL RESEARCH, VOL. 105, NO. B8, PAGES 19,067–19,083, AUGUST 10, 2000

Aftershocks of the March 9, 1994, Tonga earthquake: The strongest known deep aftershock sequence

Douglas A. Wiens

Department of Earth and Planetary Sciences, Washington University, St. Louis, Missouri

Jeffrey J. McGuire

Department of Earth, Atmospheric, and Planetary Sciences, Massachusetts Institute of Technology, Cambridge

Abstract. The March 9, 1994 (M_W 7.6, depth 564 km), deep Tonga earthquake produced an exceptionally strong aftershock sequence for a deep earthquake. Using eight temporary broadband stations deployed on the Fiji, Tonga, and Niue islands, we identify 144 aftershocks with m_b ranging from 3.2 to 6.0 during the first 41 days following the mainshock. The number and seismic moment of the March 9 aftershocks lie within the range of aftershock productivities of typical shallow earthquakes of similar moment. The aftershocks show a power law decay with time following the mainshock, with an exponent (p value) of -1.0, similar to shallow aftershock sequences. Fifty aftershocks can be accurately located using a hypocentroidal decomposition method; these aftershocks align along a near-vertical ENE striking plane similar to one of the mainshock nodal planes. Sixteen of the 18 well-located aftershocks during the first 2.5 hours are located to the NNE of the mainshock epicenter, consistent with NNE rupture propagation derived from waveform analysis. Later aftershocks are located south of the epicenter, suggesting aftershock expansion beyond the region of substantial moment release in the mainshock. Several of the aftershocks are located outside of the normal bounds of the seismically active slab, consistent with evidence that the mainshock rupture terminated outside the active slab. Five possible foreshocks occurred along the preferred fault plane within the 22 days prior to the mainshock. At least three "triggered" aftershocks occurred at distances of 50 to 110 km within the first six hours following the mainshock; triggered aftershocks in adjacent slab material may be common for large deep earthquakes. While there is some variation in the focal mechanisms of the aftershocks, most resemble the mainshock focal mechanism. All the mechanisms show compressional axes dipping to the west, consistent with background seismicity in this region. Overall, most of the aftershock characteristics of the 1994 Tonga event are similar to those found for shallow earthquakes, suggesting similarities between shallow and deep earthquakes in the mechanical processes that produce aftershocks.

1. Introduction

The aftershock properties of deep earthquakes are poorly understood, in part because substantial aftershock sequences have rarely been documented. This is partly due to the fact that deep earthquake aftershocks are less prolific than aftershocks following shallow earthquakes. Some early studies suggested that deep earthquakes may not show any aftershock sequences at all [*Page*, 1968]. Other studies noted that deep earthquake aftershocks exist but are far more sparse than shallow earthquake aftershocks [*Frohlich*, 1989].

The lack of deep earthquake aftershock sequences has limited understanding of what these aftershocks represent and how they are different from shallow earthquake aftershocks. For example, *Willemann and Frohlich* [1987] suggested that deep earthquake aftershocks were not preferentially located along mainshock nodal planes, but the largest aftershock sequences in their sample contained only six aftershocks, and the aftershocks were often not recorded by local stations. However, several recent studies have shown that intermediate and deep earthquakes can have significant aftershock sequences [*Kisslinger and Hasegawa*, 1991; *Pavlis and Hamburger*, 1991; *Wiens et al.*, 1994; *Myers et al.*, 1995]. Compilations of deep earthquake aftershock data suggest that the aftershock productivity of deep earthquakes is a function of the thermal characteristics of the slab, with the coldest slab (Tonga) showing the strongest deep earthquake aftershock sequences [*Wiens and Gilbert*, 1996]. A survey of aftershock sequences from moderate-sized deep earthquakes in the Tonga subduction zone suggests that they show an order of magnitude less aftershock activity than sequences from similar-sized mainshocks in California [*Wiens et al.*, 1997].

The March 9, 1994, earthquake (M_W 7.6, depth 564 km) occurred within the most seismic part of the deep Tonga slab, which is near vertical and strikes NW-SE (Figure 1). The mainshock focal mechanism shows largely dip-slip faulting along either a steeply dipping NNE striking fault or a nearly horizontal fault with a shallow northward dip (Figure 1). The

Paper number 2000JB900097
0148-0227/00/2000JB900097$09.00

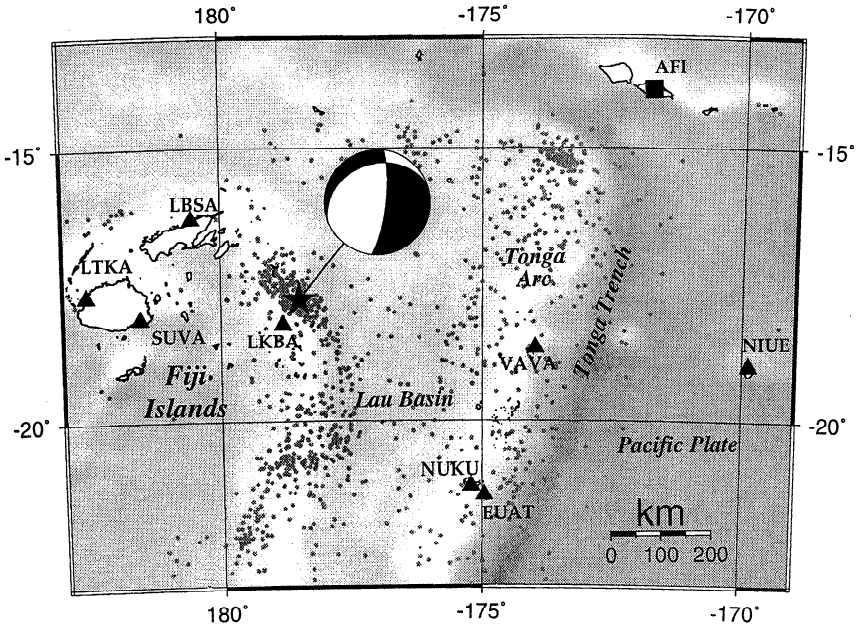

Figure 1. Locations of the March 9, 1994, Tonga deep earthquake, recording stations of the Southwest Pacific Seismic Experiment (SPASE) deployment (triangles), and the global seismic network station AFI (square). Small dots denote earthquakes from the Preliminary Determination of Epicenters (PDE) database and delineate the deep Tonga slab, and the focal mechanism is from the Harvard centroid moment tensor solution [e.g., *Dzeiwonski et al.,* 1981].

earthquake aftershock sequence was unusually energetic for a deep earthquake, and initial analysis showed that the aftershocks defined a plane that is consistent with the steeply dipping nodal plane [*Wiens et al.*, 1994]. Most analyses of teleseismic data were consistent with rupture propagation along the near-vertical fault plane [*Goes and Ritsema*, 1995; *Lundgren and Giardini*, 1995; *Tibi et al.*, 1999]. Waveform inversion of teleseismic and regional broadband data showed rupture that propagated northeastward along the steeply dipping fault for ~ 30 km at a rupture velocity of 4 km/s [*McGuire et al.*, 1997]. The rupture propagation was accompanied by a change in focal mechanism, with the fault strike rotating counterclockwise by 35° during the rupture. The rupture terminated 10-15 km outside the seismically active zone of the Tonga slab [*McGuire et al.*, 1997], near one of the aftershocks [*Wiens et al.*, 1994]. The rupture velocity (as a percent of the shear velocity) and static stress drop are similar to those of typical shallow earthquakes [*McGuire et al.*, 1997; *Tibi et al.*, 1999]

The aftershock sequence of the March 9, 1994, earthquake has several remarkable properties that make it an ideal sequence for detailed study of deep earthquake aftershock properties. First, this event produced the strongest known aftershock sequence of any deep earthquake, as measured both by the total number of aftershocks recorded and by the number of larger magnitude aftershocks [*Wiens and Gilbert*, 1996; *Wiens et al.*, 1994]. In addition, the sequence occurred fortuitously in the center of the Southwest Pacific Seismic Experiment (SPASE), a temporary deployment of eight broadband seismographs in Fiji, Tonga, and Niue Islands (Figure 1), providing high-quality records of the sequence. Finally, the mainshock occurred within the highly seismogenic northern section of the deep Tonga slab, enabling precise location of the aftershocks relative to the seismically active slab.

In this study, we analyze the statistics of this well-observed deep aftershock sequence, seeking to compare them with the accepted characteristics of shallow sequences. We also determine the spatial locations of the larger events and discuss the spatial and temporal development of the sequence. We then discuss the significance of these findings for various models of the mechanism of deep earthquakes.

2. Analysis

2.1. Event Identification

As a first step in the analysis, aftershocks were identified from the local data and added to the 20 aftershocks reported by the monthly Preliminary Determination of Epicenters (PDE) to produce a complete aftershock catalog (Table 1). Identification of all aftershocks is difficult, because of the long duration of the sequence and the high background seismicity rate of the Tonga subduction zone. Because the aftershock occurrence rate shows a power law decay with time, small events with imprecise locations determined in the first few hours after the mainshock are much more likely to be aftershocks than events recorded later in the sequence. Therefore we used different methods and criteria for identifying aftershocks at different time periods in the sequence. These different methods render the aftershock catalog non-uniform in time, but this can be corrected for study of the temporal characteristics by considering only events above a magnitude cutoff where detection is likely to be uniform.

During the first 10 days of data following the mainshock, we identified aftershocks interactively by examining filtered three-component data from the Fiji and Tonga stations showing the best signal-to-noise ratios (LBSA and VAVA). For the later part of the sequence, we used an automated procedure that identified arrivals from the ratio of the short-

Table 1. Aftershocks of the March 9, 1994, Tonga Earthquake

Event	Month	Day	Origin Time, (UT)	Number of arrivals	m_b	Latitude	Longitude	Depth (km)	Uncert-ainty (km)[a]
Main	3	9	2328:08	258	6.6	-18.05	-178.22	565.	2.4
1	3	9	2330:44	6	4.8				
2	3	9	2332:00	2	4.4				
3	3	9	2333:30	2	4.2				
4	3	9	2333:43	6	4.9				
5	3	9	2335:23	4	4.3				
6	3	9	2336:28	10	4.8	-17.98	-178.13	557.	8.9
7	3	9	2336:56	4	4.3				
8	3	9	2338:15	2	3.9				
9	3	9	2338:54	11	4.5	-17.77	-178.13	580.	10.8
10	3	9	2340:14	4	4.7				
11	3	9	2341:00	10	5.0	-18.17	-178.18	551.	9.3
12	3	9	2343:58	4	3.8				
13	3	9	2347:00	2	3.5				
14	3	9	2347:15	2	3.6				
15	3	9	2349:16	3	3.8				
16	3	9	2350:25	102	6.0[b]	-17.93	-178.13	579.	2.7
17	3	9	2352:13	8	4.5	-17.94	-178.12	568.	11.5
18	3	9	2353:31	16	5.0	-17.91	-178.09	574.	6.1
19	3	9	2354:08	10	5.0	-17.88	-178.03	552.	9.1
20	3	9	2354:37	3	4.4				
21	3	9	2359:01	3	3.3				
22	3	9	2359:23	4	3.9				
23	3	9	2359:45	3	3.6				
24	3	10	0003:43	5	3.7				
25	3	10	0004:21	4	3.9				
26	3	10	0005:12	3	3.9				
27	3	10	0005:32	4	3.7				
28	3	10	0005:56	12	4.5	-17.95	-178.21	557.	6.7
29	3	10	0007:27	3	3.8				
30	3	10	0009:27	7	3.6				
31	3	10	0012:50	11	4.4	-17.92	-178.10	591.	8.9
32	3	10	0013:14	3	3.6				
33	3	10	0015:01	4	3.9				
34	3	10	0018:01	3	3.6				
35	3	10	0023:55	19	4.8	-17.99	-178.17	563.	4.6
36	3	10	0027:22	7	3.7				
37	3	10	0028:18	3	3.7				
38	3	10	0029:12	6	4.0				
39	3	10	0033:24	7	4.1				
40	3	10	0035:20	3	4.0				
41	3	10	0038:31	3	3.6				
42	3	10	0044:51	4	3.9				
43	3	10	0050:26	12	4.5	-18.18	-178.30	574.	10.2
44	3	10	0113:28	6	3.9				
45	3	10	0114:35	8	4.1	-17.79	-178.09	554.	11.6
46	3	10	0117:30	8	3.8	-17.82	-178.17	560.	10.1
47	3	10	0119:23	4	3.7				
48	3	10	0120:59	5	3.8				
49	3	10	0133:57	5	3.6				
50	3	10	0136:58	4	3.6				
51	3	10	0145:38	4	3.9				
52	3	10	0150:12	4	3.7				
53	3	10	0155:06	5	3.7				
54	3	10	0203:10	4	3.7				
55	3	10	0207:22	4	3.8				
56	3	10	0213:01	8	3.9	-17.99	-178.16	578.	12.4
57	3	10	0230:06	4	3.8				
58	3	10	0231:48	10	4.1	-17.72	-178.19	541.	11.4
59	3	10	0232:55	10	4.6	-17.83	-178.14	565.	11.0
60	3	10	0236:40	7	4.0				
61	3	10	0238:39	7	3.8				
62	3	10	0244:20	27	4.8[b]	-17.91	-178.19	556.	4.3
63	3	10	0251:28	5	3.8				
64	3	10	0259:50	8	3.9	-18.25	-178.32	553.	7.4

Table 1. (continued)

Event	Month	Day	Origin Time, (UT)	Number of arrivals	m_b	Latitude	Longitude	Depth (km)	Uncert-ainty (km)[a]
65	3	10	0346:22	44	4.2[b]	-18.08	-178.24	557.	3.5
66	3	10	0355.01	4	3.8				
67	3	10	0403:10	45	5.0[b]	-17.98	-178.16	569.	3.6
68	3	10	0453:01	6	3.6				
69	3	10	0456:32	4	3.4				
70	3	10	0524:10	6	4.0				
71	3	10	0552:59	5	3.5				
72	3	10	0702:27	5	3.7				
73	3	10	0744:46	15	4.2	-17.66	-178.22	554.	6.7
74	3	10	0959:43	16	4.1[b]	-17.90	-178.10	558.	7.4
75	3	10	1029:28	68	4.9[b]	-18.17	-178.24	574.	3.0
76	3	10	1048:33	4	4.0				
77	3	10	1100:15	5	4.2				
78	3	10	1121:36	6	4.1				
79	3	10	1225:44	170	5.2[b]	-18.05	-178.12	596.	2.6
80	3	10	1323:14	23	4.4[b]	-18.03	-178.18	567.	6.8
81	3	10	1348:37	3	3.5				
82	3	10	1351:15	8	4.3				
83	3	10	1414:22	27	4.4[b]	-18.32	-178.35	583.	4.1
84	3	10	1434:58	4	3.8				
85	3	10	1519:54	6	3.4				
86	3	10	1612:15	5	3.7				
87	3	10	1651:34	4	3.4				
88	3	10	1827:18	6	4.2				
89	3	10	1908:46	83	4.5[b]	-18.04	-178.28	557.	3.2
90	3	10	2056:35	4	3.9				
91	3	10	2201:00	6	4.3				
92	3	10	2311:41	8	4.3	-18.14	-178.39	565.	8.0
93	3	11	0209:42	4	3.8				
94	3	11	0303:25	13	4.6	-18.18	-178.38	562.	6.4
95	3	11	0310:05	4	3.6				
96	3	11	0547:30	6	3.9				
97	3	11	1043:46	5	3.4				
98	3	11	1345:04	6	3.8				
99	3	11	1646:23	8	4.1	-18.11	-178.20	581.	10.9
100	3	12	1414:40	9	4.4	-17.99	-178.16	558.	7.3
101	3	12	1440:03	5	3.5				
102	3	12	1448:49	5	3.3				
103	3	12	1641:23	6	3.4				
104	3	12	1745:01	7	3.6				
105	3	13	1142:10	5	3.3				
106	3	13	1428:53	7	3.5				
107	3	14	0846:32	7	4.3				
108	3	14	1012:52	5	3.2				
109	3	14	1114:42	4	3.4				
110	3	14	1809:19	8	4.0	-18.08	-178.26	559.	7.3
111	3	14	2252:15	10	4.2	-18.23	-178.32	602.	7.2
112	3	15	1330:09	5	3.3				
113	3	15	1912:28	6	3.8				
114	3	16	0529:01	9	4.3	-18.11	-178.26	556.	6.8
115	3	16	1017:07	6	3.6				
116	3	16	2059:45	6	4.0				
117	3	16	2254:19	6	3.6				
118	3	18	0836:10	10	4.1	-18.00	-178.08	560.	12.0
119	3	18	0939:57	7	3.5				
120	3	18	1245:02	4	3.5				
121	3	18	1822:01	8	4.0	-17.91	-178.13	547.	11.2
122	3	24	1717:21	41	4.7[b]	-18.03	-178.05	584.	4.0
123	3	25	2317:56	82	5.3[b]	-17.79	-178.30	571.	3.2
124	3	27	1042:38	7	3.9				
125	3	27	1047:35	46	4.7[b]	-17.93	-178.10	579.	5.3
126	3	27	1120:41	87	5.1[b]	-17.79	-178.03	571.	3.2
127	3	27	1439:49	8	3.8				
128	3	28	0612:44	5	4.1				
129	3	28	1337:46	4	3.9				
130	3	30	0820:03	6	3.9				

Table 1. (continued)

Event	Month	Day	Origin Time, (UT)	Number of arrivals	m_b	Latitude	Longitude	Depth (km)	Uncert-ainty (km)[a]
131	4	2	1318:28	22	4.7[b]	-17.80	-178.05	588.	5.8
132	4	2	2149:56	7	4.1				
133	4	3	0909:05	8	4.1				
134	4	4	1300:05	6	4.2				
135	4	5	0522:27	8	4.2	-17.94	-178.11	574.	8.6
136	4	5	1346:49	7	3.8				
137	4	6	0455:35	25	4.2[b]	-18.13	-178.29	570.	4.1
138	4	15	0758:01	6	4.0				
139	4	20	0005:10	7	4.0				
140	4	20	1633:04	10	4.2	-18.26	-178.25	592.	6.3
141	4	20	2335:31	209	5.6[b]	-17.94	-178.22	548.	3.0

[a] Average length of the three semi-axes of the 95% confidence ellipsoid for the relative position of the earthquake.
[b] m_b from the Preliminary Determination of Epicenters (PDE)

term average and the long-term average of the amplitude of the filtered traces. This same procedure was used to identify earthquakes throughout the 1993-1995 SPASE deployment, thus providing some estimate of the background seismicity in this region. The interactive procedure is somewhat better for identifying very small events recorded by only a few stations.

Immediately after the mainshock, scattered energy makes location of aftershocks difficult, but any observed high-frequency arrivals are likely to be aftershocks. We therefore required two consistent arrivals to identify an aftershock during the first 30 minutes following the mainshock and required three consistent arrivals during the next hour. For the first 20 days following the mainshock we required a location within 60 km of the mainshock obtained from at least four arrivals. During the later parts of the sequence, contamination of the aftershock sequence by background seismicity is a significant problem, and we require that the event have a well constrained location in the immediate vicinity of the mainshock fault plane determined by at least six arrivals.

Determining the termination time of an aftershock sequence is generally difficult, since the event occurrence rate returns to the normal background rate very slowly. We estimate the background seismicity rate from the number of events detected during the rest of 1994 by the SPASE array within 50 km of the March 9 hypocenter and obtain 0.19 events/day. The aftershock seismicity rate remained well above this level until at least April 20, 41 days after the mainshock. We thus limit our analysis to this time period.

The aftershock sequence contains several events that were triggered outside the immediate region of the mainshock (Table 2). One of the largest aftershocks of the March 9 sequence (March 10, 0151 UT, m_b 5.0, 637 km) was clearly a triggered event, located ~ 70 km beneath the mainshock, well outside the rupture zone. It occurred within three hours of the mainshock in a location with little background seismicity. Two other events occurred ~ 110 km southeast of the mainshock within the first six hours and probably also represent triggered aftershocks. The long-term seismicity rate for teleseismically located earthquakes $m_b \geq 4.5$ within

Table 2: Other Events associated with the March 9 Tonga Earthquake

Month	Day	Origin Time, (UT)	m_b	Latitude	Longitude	Depth, km	Number of arrivals	Uncer-tainty, km
			Possible Foreshocks					
2	15	19:02:44	4.7[a]	-18.13	-178.33	570.	33	4.9
2	17	22:40:57	5.2[a]	-18.15	-178.22	591.	27	7.8
2	26	13:18:05	4.0	-18.20	-178.30	602.	12	8.6
3	2	14:32:43	-	-17.94	-178.26	559.	8	8.1
3	2	23:58:02	4.3	-17.70	-178.08	540.	21	4.1
3	6	06:37:14	4.3[a]	-18.32	-178.00	575.	30	5.0
			Triggered Events					
3	10	00:43:08	5.2[a]	-18.89	-177.76	609.	48	4.5
3	10	01:51:41	5.0[a]	-18.04	-178.24	637.	151	2.9
3	10	04:49:57	4.7[a]	-18.91	-177.70	615.	43	3.8

[a] m_b from PDE

130 km of the March 9 epicenter is about one event per eight days, so the probability of three random background events occurring within six hours of the March 9 mainshock is low.

Using this procedure, we compile a list of 141 aftershocks not counting the triggered events, with the first one occurring 2.5 minutes and the final one 41 days following the mainshock (Table 1). This is by far the most aftershocks identified for any deep earthquake, with only the 1994 Bolivia event (M_W 8.3), with 87 [*Myers et al.*, 1995], and the 1996 Flores Sea event (M_W 7.8), with 33 [*Wiens and Gilbert*, 1996], as close competitors. Both of these earthquakes were significantly larger than the 1994 Tonga event. Several smaller deep events in the Tonga and Mariana subduction zones have also been identified as having unusually large aftershock sequences [*Wiens and Gilbert*, 1996; *Wu and Chen*, 1999], but these events have a much smaller total number of aftershocks.

There was also considerable activity near the March 9 event within 22 days prior to the earthquake (Table 2), although the high level of background seismicity renders it uncertain whether these events represent foreshocks or fortuitous background events. The level of foreshock activity (six events within 22 days) provides a rate of 0.27 events/day, as compared to a seismicity rate of 0.19 events/day within 50 km of the epicenter for the rest of 1994, suggesting that the events may represent background seismicity. However, four of the possible foreshocks have well-constrained locations along the fault plane, suggesting that they are linked to the mainshock.

2.2. Magnitude Determination

We developed an empirical procedure for determining body wave magnitudes that are compatible with standard PDE m_b determinations. The m_b values are computed from:

$$m_b = \log (A/T) + f(h, \Delta) \quad (1)$$

where A is amplitude, T is period, and $f(h, \Delta)$ is a function of source depth (h) and epicentral distance (Δ). If all the earthquakes are from the same limited source region and the amplitude measurements are made at approximately the same period, then $f(h, \Delta)$ will be identical for all earthquakes observed at a given station. In this case the equation reduces to

$$m_b = \log (A) + C_N \quad (2)$$

where C_N is an empirical constant appropriate for the given source-station geometry and period.

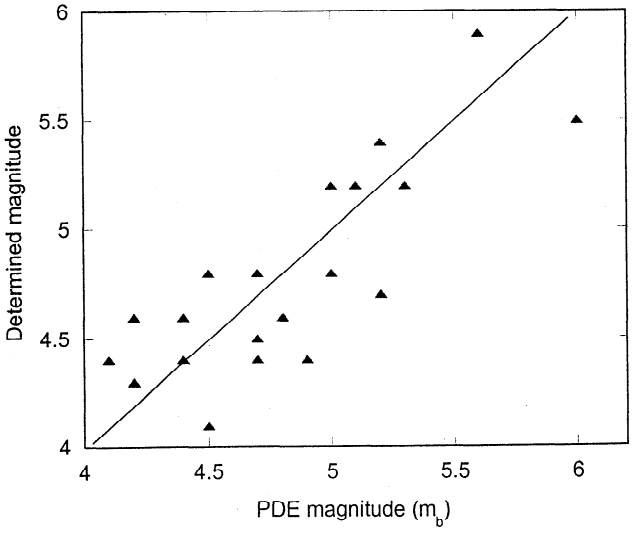

Figure 2. Plot of magnitude determined from amplitudes at SPASE stations using the procedure used in this study as a function of PDE magnitudes. A line through the origin with a slope of 1 is also shown. The magnitude determination procedure used here successfully reproduces the PDE magnitudes, with a scatter of about 0.3 magnitude units.

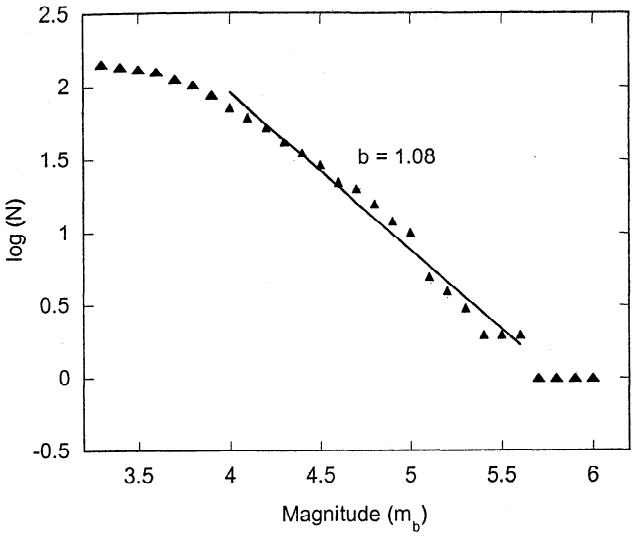

Figure 3. Magnitude-frequency characteristics of the March 9 aftershock sequence. The falloff of the seismicity for low magnitudes suggests that the limit for uniform detection is ~ 4.0. A least squares fit to the seismicity between m_b 4.0 and 5.6 suggests a b value of 1.08 $\pm$ 0.04.

We determined the empirical constant C_N for each station from a least squares fit to the observed amplitudes determined from the regional broadband seismograms. The observed waveforms were band-pass filtered with a center frequency of 2 Hz prior to amplitude determination. The earthquake data set for this fit consisted of the aftershocks for which a PDE magnitude is available and other earthquakes during 1994 that were within 60 km of the March 9 hypocenter. Magnitude estimates were then determined for each station using equation (2), and these magnitudes were averaged to obtain magnitude estimates for each event. One advantage of this process is that the derived magnitudes are compatible with those determined by the PDE, and we adopt the PDE magnitudes for events in the PDE catalog. For these events the magnitudes determined using the procedure described here reproduce the PDE magnitudes with a scatter of about 0.3 magnitude units (Figure 2). This scatter is probably due to uncertainties in both magnitude determination procedures due to wave propagation and source radiation pattern effects. The final magnitudes for all the aftershocks are listed in Table 1 and range from 3.2 to 6.0.

The aftershock sequence shows a typical magnitude-frequency relation. The magnitude frequency observations deviate from a linear relation for magnitudes smaller than 4.0, suggesting that this represents the approximate limiting magnitude above which most of the aftershocks are detected (Figure 3). We therefore perform a linear least squares fit to

the magnitude-frequency data between magnitudes of 4.0 and 5.6 and obtain a slope (b value) of 1.08 $\pm$ 0.04.

2.3. Aftershock Decay With Time

The Tonga sequence shows a rapid decrease in activity with time, such that most of the aftershocks are observed during the initial 24 hours after the mainshock. We analyzed the temporal decay of seismicity in order to compare it with results from shallow earthquakes. For the temporal analysis we use only the 103 aftershocks with $m_b \geq 3.8$, since the smallest earthquakes were not detected uniformly during the sequence.

We assume that the decay follows the modified Omori formula [*Utsu*, 1961]:

$$n(t) = K (t + c)^{-p} \quad (3)$$

where $n(t)$ represents the number of aftershocks per unit time, K is proportional to the total number of events in the sequence, c is the time interval at the beginning of the sequence during which aftershocks are poorly recorded, and p is often thought to be related to the physical setting of the earthquake sequence [*Kisslinger*, 1996]. We solve for the constants K, C, and p using a maximum likelihood method [*Ogata*, 1983] and obtain K= 11.8, c = 3.5 min, and p = 1.006.

Figures 4 and 5 show the fit of the temporal data set to equation (3). Figure 4 shows the data from the first day following the mainshock plotted in bins of 1-hour duration. The power law decay with p=1.006 provides an excellent fit to the data, except for minor surges in aftershock activity about 3 hours (March 10; 0230 UT) and 11 hours (March 10; 1029 UT) following the mainshock. This is similar to the results of *Nyffenegger and Frohlich* [2000] for this event. They used the list of event times from this study but could not use a magnitude threshold to ensure uniform detection with time.

The temporal behavior of the later part of the sequence is better shown on a log-log plot of the aftershock rate as a function of time (Figure 5). The aftershock rates for the entire sequence are well fit by a power law decay which is linear on the log-log plot, and the aftershock rates approach the background seismicity rate at about 1000 hours (~42 days), the duration we estimate for the sequence. A least squares exponential fit to this data suggests a decay exponent (p) of 1.017, consistent with the maximum likelihood estimate (1.006). We prefer the maximum likelihood estimate because it does not require a priori binning of the data and includes the parameter c from the modified Omori formulation.

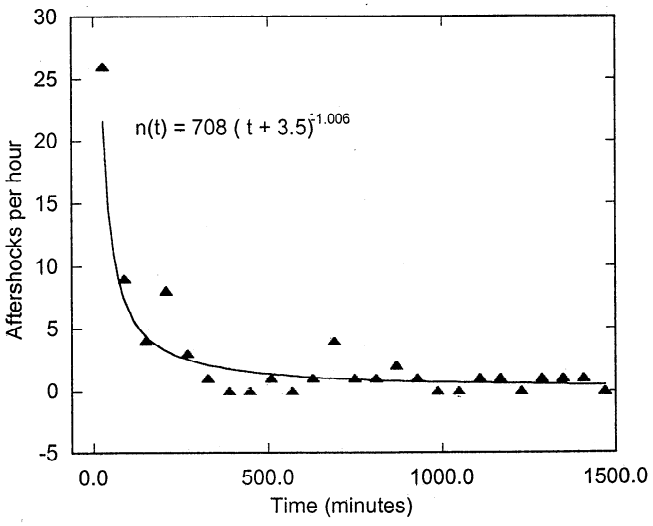

Figure 4. Temporal decay of the aftershock occurrence rate for aftershocks with $m_b \geq 3.8$ during the first day following the 1994 Tonga deep earthquake. The line shows the fit obtained from a maximum likelihood analysis of the entire sequence.

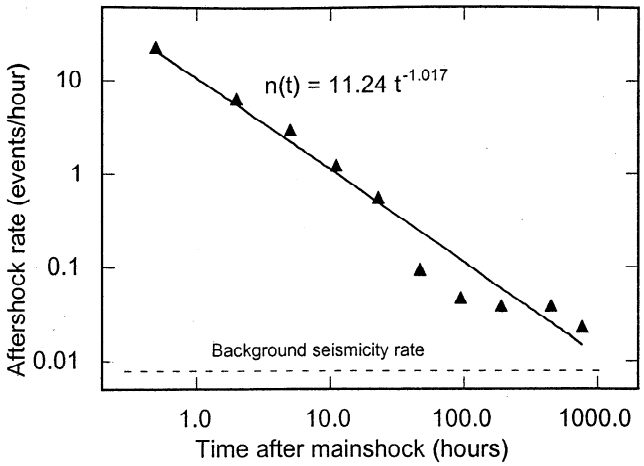

Figure 5. Temporal decay of the aftershock occurrence rate for the entire 41 day aftershock sequence on a log-log plot. The aftershock occurrence rate is determined within bins that increase in duration as the sequence progresses. The decay exponent (1.017) is determined from a least squares exponential fit to this binned dataset. The background seismicity rate (0.008 events/hr) is determined by examining seismicity within 50 km of the epicenter during the remainder of 1994.

2.4. Aftershock Location Determination

We study the spatial configuration of the aftershocks using a hypocentroidal decomposition location algorithm developed by *Jordan and Sverdrup* [1981]. This method uses arrival times from different earthquakes for the same seismic phase and station to constrain earthquake relative positions within a limited source region, thus minimizing the effect of velocity heterogeneity along the ray paths.

The arrival time dataset consists of direct P and S arrival times picked from the local broadband stations, as well as P and pP arrival times reported to the PDE. We also picked arrival times directly from digital data from the station AFI in Samoa and picked a small number of teleseismic arrivals from global digital broadband stations in other parts of the southwest Pacific. Standard deviations ranging from 0.2 to 1.0 s are estimated for each pick from the local stations and used in the location determination. The PDE arrival times are generally less accurate than the arrival times determined from the local stations, and are assigned a value of 0.75 s for direct P phases and 1.0 s. for pP phases, as derived from the residual statistics. The solutions for the larger events show small uncertainties, resulting from the combination of highly accurate local observations with numerous teleseismic observations.

The locations of all aftershocks with at least eight arrival times were determined in a simultaneous inversion using the

above procedure. The location of each of these 48 events is given in Table 1, along with the approximate uncertainty, which is the average length of the three semiaxes of the 95% confidence ellipsoid. The locations of possible foreshocks and triggered aftershocks are given in Table 2. The location uncertainties of some of these events are quite large, so a higher-quality data set for visualization of earthquake locations was generated by eliminating events with less than 10 arrival times or with large location uncertainties. Most of the discussion is based on this data set of 34 high-quality locations.

The positions of the aftershocks relative to the background seismicity were determined using a joint inversion of the aftershocks along with a data set of 1980-1995 earthquakes. About half of these earthquakes occurred during the remainder of the 1993-1995 SPASE deployment, and were thus well recorded by the same set of local stations as well as teleseismic stations. All of these events have at least 14 arrival times. The other half of the data set consists of 1980-1993 earthquakes with at least 50 arrival times in the International Seismological Centre (ISC) database. All events showing average 95% confidence semiaxis lengths of greater than 8 km were eliminated from the inversion. The final relocation consisted of 27,200 arrival times from 297 events within ~ 90 km of the mainshock.

2.5. Source Parameter Determination

A number of the aftershocks were large enough that their focal mechanisms could be determined using a combination of the regional broadband data from the SPASE deployment and teleseismic broadband data from the Global Seismic Network (GSN). The aftershocks show a variety of focal mechanisms, as could immediately be inferred from the variable *P* and *S* polarities and wave shapes at the regional seismic stations (Figure 6). Two methods were used to determine focal mechanisms for the aftershocks. Focal mechanisms of the larger events were determined by inversion of *P* and *S* waveforms using a grid search method. Synthetic seismograms were calculated using a reflectivity method [*Kennett*, 1983], and synthetics for arbitrary focal mechanisms were calculated by linear combinations of fundamental synthetic seismograms [*Langston and Helmberger*, 1975].

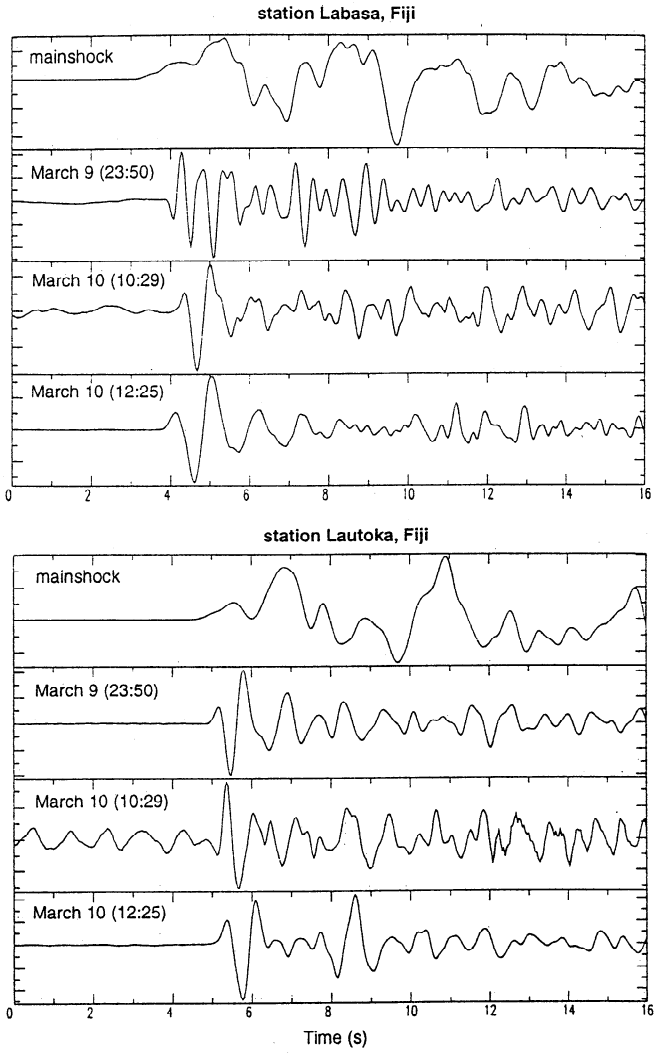

Figure 6. *P* waveforms at recorded at regional broadband stations LBSA and LTKA for the mainshock and several aftershocks. The aftershock records have been filtered with a 1-Hz high-pass filter that preserves the initial polarity; raw broadband records are shown for the mainshock. The different polarities illustrate the variability of the focal mechanisms for the aftershocks.

Table 3. Focal Mechanisms

Date	Time, UT	Strike, deg	Dip, deg	Slip, deg	Moment, 10^{17} N-m	Duration, s	Source[a]
March 9	23:28:08	8	76	252	3100	13	M
	subevent 1	25	65	240			M
	subevent 2	5	80	235			M
	subevent 3	355	80	235			M
March 9	23:50:25	70	45	220	-	-	G
March 10	1:51:41	80	45	220	-	-	G
March 10	3:46:22	20	45	270	-	-	G
March 10	10:29:28	55	90	200	-	-	G
March 10	12:25:44	30	75	280	1.4	1	W
March 10	19:08:46	25	70	260	-	-	G
March 24	17:17:21	25	78	285			G
March 25	23:17:56	0	85	230	-	-	G
March 27	11:20:41	16	72	248	0.9	2	W
April 20	23:35:31	42	76	262	11	5	W

[a]Sources of focal mechanism determination are M, waveform inversion from *McGuire et al.* [1997]; W waveform inversion from this study; G, grid search fit to *P* and *S* wave first motions and *S* polarization data from this study.

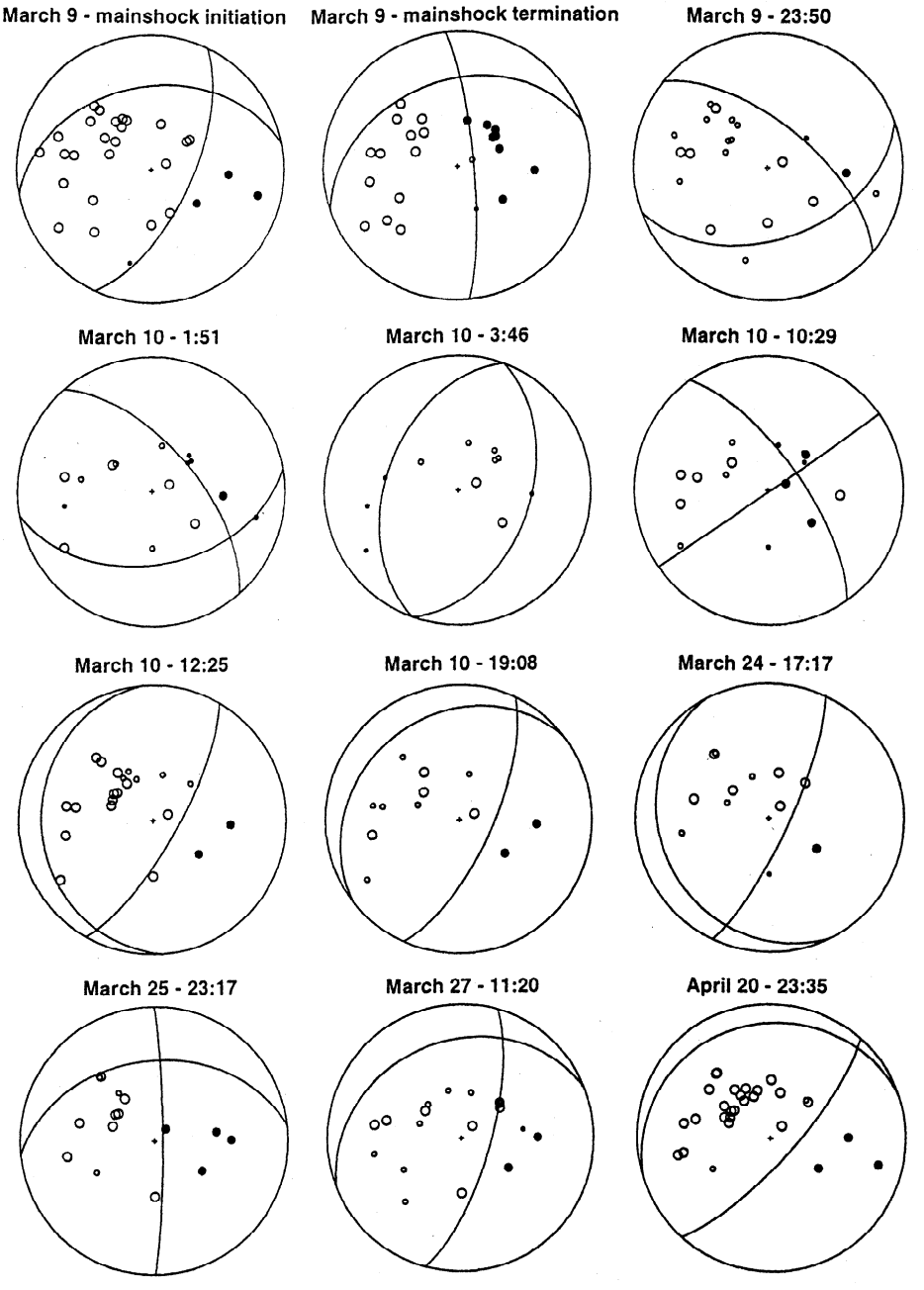

Figure 7. Focal mechanisms for the mainshock and aftershocks of the March 9, 1994, event (Table 3). Focal mechanisms for the initiation and termination of the March 9 mainshock are from *McGuire et al.* [1997]; focal mechanisms for the aftershocks are from this study. Focal mechanisms are shown as lower hemisphere projections, with observed compressional P wave first motions shown as solid circles and dilatational first motions as open circles. Larger symbols denote higher-quality picks. Note that the March 10 (0151 UT) and March 25 (2317 UT) aftershocks were not located along the mainshock fault plane.

The raw broadband data and synthetics were filtered using a 0.02 to 0.12 Hz band-pass filter to provide a good signal-to-noise ratio.

Smaller aftershocks did not show good signal-to-noise ratios at frequencies suitable for waveform inversion. Focal mechanisms were determined for these events from *P*, *SV*, and *SH* first motions and *S* wave polarizations. Each observation was assigned a quality rating ranging from A to C. In the final analysis, observations with a quality rating of C were not used, and qualities of A were assigned twice the weight of the B observations. *P* wave polarities were obtained from both regional and teleseismic observations, but *S* wave observations were obtained only from regional stations. The focal mechanisms obtained from the waveform inversion are more accurately determined than those obtained from the grid search procedure. Uncertainties for the focal mechanism parameters (strike, dip, slip) are of the order of 5° to 10° for the waveform inversion, in contrast to uncertainties of 15° to 20° for the grid search procedure.

The focal mechanisms are compiled in Table 3. Events on March 10 (1225 UT), March 27, and April 20 were large enough for waveform analysis, whereas focal mechanisms for the other aftershocks were determined using the grid search fit to the first motions and *S* wave polarizations. Seismic

moments and source durations are also tabulated for the events studied using waveform inversion. *P* wave focal mechanisms along with *P* wave first motion polarities are shown in Figure 7.

3. Results and Discussion

3.1. Statistical Comparison With Typical Shallow Aftershock Sequences

Differences in aftershock productivity and characteristics are among the most frequently cited differences between shallow and deep earthquakes, and thus may provide important clues about the mechanism of deep earthquakes. The March 9 sequence may provide the first real opportunity to compare a robust deep earthquake aftershock sequence with the well-known characteristics of typical shallow aftershock sequences.

3.1.1. Aftershock productivity. Since the March 9 sequence is the strongest known deep aftershock sequence, it is natural to question how the aftershock productivity of this sequence compares to typical shallow earthquakes. Table 4 compares the aftershock productivity of the 1994 Tonga deep earthquake with the characteristics of typical shallow earthquakes of similar size, obtained by analyzing all 14 shallow earthquakes with moments between 1.5 and 5 x 10^{20} N-m during 1990-1996. The aftershock productivity is compared using the total number of aftershocks with $m_b \geq 4.5$ in order to reduce the effects of regional detection thresholds. Aftershock productivity is also compared using the ratio of total aftershock moment to mainshock moment. Since the aftershock moment sum is generally dominated by a few of the largest earthquakes, we estimate the total aftershock moment by summing the moments of the eight largest aftershocks.

Table 4 shows that the 1994 deep Tonga aftershock sequence is weaker, both in total number of aftershocks and in total seismic moment, than typical shallow earthquakes of similar mainshock moment. The aftershock moment release is ~ 3% of the mainshock moment release for a typical shallow earthquake, as compared to 1.4% for the 1994 sequence. The total number of aftershocks is ~ 3 times larger for shallow earthquakes. However, shallow earthquakes show a large scatter in productivity, and the 1994 deep Tonga sequence exceeds some of the weaker shallow sequences in both measures of aftershock productivity. Thus the aftershock productivity of the 1994 deep Tonga sequence is at the low end of the normal range found for shallow earthquakes.

As the 1994 Tonga sequence is the most prolific deep earthquake in aftershock production, this conclusion does not apply to deep earthquakes generally. However, deep earthquake aftershock productivity is inversely correlated with the temperature of the subducting slab [*Wiens and Gilbert,* 1996]. The largest previous deep Tonga earthquake, on May 26, 1932 (M_W 7.6), also showed an active aftershock sequence despite the limited instrumentation of that time [*Okal,* 1997]. Thus the aftershock statistics of the 1994 Tonga event might be relatively typical of large deep earthquakes in cold slabs.

3.1.2. Magnitude-frequency relation. The observed magnitude-frequency relation (*b* value) of 1.08 $\pm$ 0.04 (Figure 3) is similar to the *b* value of 1.23 (for m_b) observed for the entire global dataset of shallow earthquakes [*Frohlich and Davis*, 1993]. It is also indistinguishable from the average *b* value of California aftershock sequences of 1.06 [*Kisslinger and Jones*, 1991], demonstrating that this sequence is basically identical to shallow sequences in its magnitude-frequency characteristics. It is also similar to the *b* value of the March 31, 1994 (M_W=6.5, depth 585 km) Tonga sequence (*b*=1.1 $\pm$ 0.1) [*Wiens et al.*, 1997] which was also observed by the SPASE deployment. However, the *b* value is much less than the *b* value of 1.6 observed for the entire population of teleseismically recorded deep earthquakes in Tonga [*Frohlich and Davis*, 1993], suggesting that individual deep aftershock sequences in Tonga may show lower *b* values than the deep earthquake population as a whole.

3.1.3. Temporal decay. The decay of this sequence in time is indistinguishable from an average shallow sequence. We find a decay constant (*p* value) of 1.006, consistent with average values found for California earthquakes [*Kisslinger and Jones*, 1991] of 1.11 $\pm$ 0.25 and with most studies of *p* values for shallow earthquakes which suggest *p* = 1.0 to 1.3 [*Davis and Frohlich*, 1991]. A comprehensive study of all shallow sequences in global catalogs suggests an average global value of 0.868 [*Davis and Frohlich*, 1991]. The *p* value that we find is not consistent with a previous estimate of *p* values for intermediate and deep earthquakes, 0.539 [*Davis and Frohlich*, 1991], which was from analysis of a global catalog that contained no strong aftershock sequences. However, our results are consistent with those of *Nyffenegger and Frohlich* [2000], who studied several deep earthquake aftershock sequences, including this event as well as the 1994 Bolivia event.

The *p* value found by this study is particularly significant, since prior studies have suggested that *p* values are indicative of the physical characteristics of the source region. For

Table 4. Comparison of the 1994 Tonga Sequence with Shallow Aftershock Sequences

	Mainshock Moment, 10^{20} N-m	Aftershocks, $m_b \geq 4.5$	Aftershock/Mainshock Moment Ratio[a]
1994 deep Tonga sequence	3.1	29	0.014
Median, 14 shallow earthquakes[b]	3.3	84	0.031
Range, 14 shallow earthquakes	1.6 – 4.9	18-150	0.0014 – 0.203

[a] Aftershock moment sum estimated by adding the moments of the eight largest aftershocks; moments were estimated for aftershocks with no CMT or waveform solutions using *Okal and Romanowicz* [1994].

[b] Typical shallow earthquake statistics were obtained from PDE and Harvard CMT solutions [e.g. *Dziewonski et al.,* 1981] for all 14 shallow earthquakes with seismic moments between 1.5-5 x 10^{20} N-m during 1990-1996

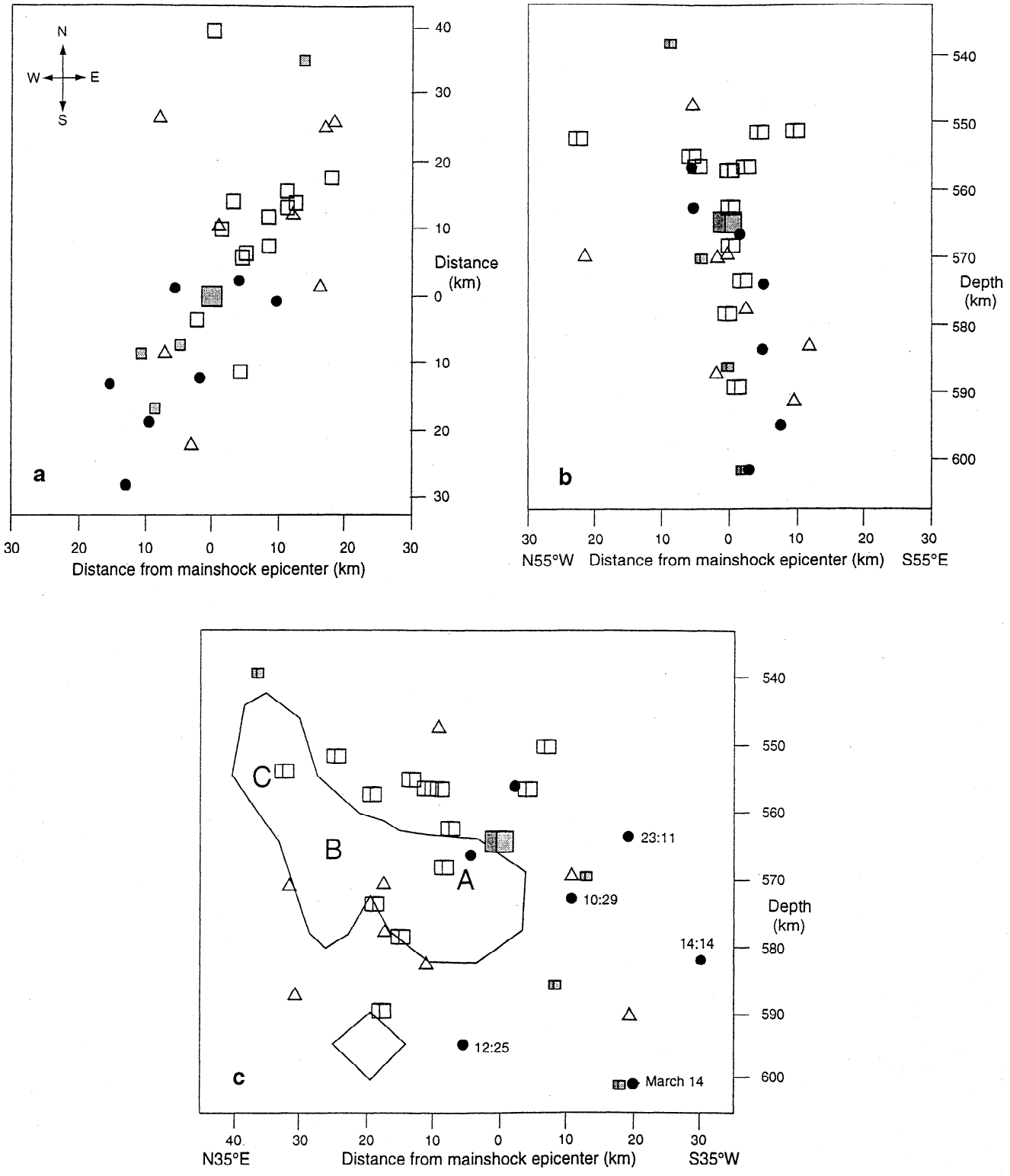

Figure 8. Foreshock, mainshock, and aftershock locations determined by a hypocentroidal decomposition inversion of local and teleseismic arrival times. Only events with more than 10 arrivals and with average 95% confidence semiaxes of less than 10 km are shown. The mainshock is shown as a large shaded cube, foreshocks are shown as small shaded cubes, early aftershocks (within the first 11 hours) are shown as unshaded cubes, later aftershocks (from 11 hours to 5 days following the mainshock) are shown as solid circles, and the latest aftershocks (from 6 to 42 days) are denoted by triangles. (a) Top (map) view, (b) view looking horizontally from N35°E, edge-on to the planar distribution of aftershocks. (c) view looking horizontally from N55°W, broadside to the planar aftershock distribution. The region of high slip during the mainshock rupture as determined by waveform inversion [*McGuire et al.*, 1997] is shown, and origin times are given for aftershocks between 11 hours and 5 days following the mainshock, which define an area of aftershock expansion to the south.

example, p values in several places seem to correlate with surface heat flow, with high heat flow regions showing much higher p values of ~ 1.35 [*Kisslinger*, 1996]. Several theoretical studies predict different p values for regions of different mechanical properties. *Mikumo and Miyatake* [1979] suggest that greater shear strength heterogeneity in the near-source region produces smaller p values. The fact that the temporal decay characteristics of the deep Tonga earthquake are similar to average shallow events suggests that some of the mechanical and statistical properties of the faulting process may be similar.

3.1.4. Triggered events and foreshocks. Large shallow earthquakes occasionally trigger aftershocks at large distances [*Hill et al.*, 1993; *King et al.*, 1994; *Gomberg et al.*, 1997]. The aftershocks at 0043, 0151, and 0449 UT on March 10 represent events that were probably triggered at distances of 70–100 km from the mainshock. The timing of the triggered events does not correspond with the passage of major seismic phases that could cause small stress perturbations. These three remote aftershocks demonstrate that deep earthquakes can trigger aftershocks at distances well removed from the actual mainshock rupture plane. Triggered remote aftershocks have also been noted other large deep earthquakes. For example, the largest aftershock of the 1994 Bolivia earthquake (M_W=8.3, 636 km) was at a distance of 300 km about 10 min after the mainshock [*Myers et al.*, 1995]. Remote triggering of aftershocks may be quite common among deep earthquakes.

It is not known whether deep earthquakes show foreshocks. The March 9 sequence shows four events with well-constrained locations along the fault plane within 22 days prior to the mainshock (Table 2). This level of activity along the eventual fault plane is certainly higher than would be expected by chance and suggests foreshock activity.

3.2. Aftershock Locations and the Mainshock Rupture

The positions of the mainshock and the 29 best located aftershocks show that the aftershocks delineate a near-vertical planar surface (Figure 8). This result had previously been noted by locating the 14 largest aftershocks [*Wiens et al.*, 1994]. The least squares best fit plane determined from these 29 locations has strike 37° and dip 62°, which is similar to the orientation (strike 25°, dip 66°) of the near-vertical fault plane of the focal mechanism corresponding to the onset of rupture [*McGuire et al.*, 1997]. The close correspondence of the plane of aftershocks with one of the mainshock nodal planes clearly indicates that the mainshock ruptured on the near-vertical nodal plane.

Comparison of the positions of the aftershocks with the spatial location of the areas of high slip during the mainshock reveals some interesting insight into the development of the aftershock sequence. Nearly all of the aftershocks during the first 11 hours after the mainshock, including 16 of the 18 well-located aftershocks during the first 2.5 hours, are located in or near zones of high slip during the mainshock (Figure 8b), as determined by waveform inversion [*McGuire et al.*, 1997]. Most of these are concentrated along a line extending northeastward and slightly upward from the hypocenter, consistent with source studies of this event, which show dominantly northward rupture propagation [*Goes and Ritsema*, 1995; *Lundgren and Giardini*, 1995; *McGuire et al.*, 1997]. There also seems to be a tendency for the early aftershocks to be located around the edges of the regions of highest slip (Figure 8c). This phenomenon has been previously noted for shallow earthquake sequences [*Mendoza and Hartzell*, 1988; *Dreger*, 1997], and is commonly attributed to either a near total relaxation of stress in the high slip regions or stress loading within the region surrounding the high slip region.

Beginning with larger aftershocks at 1029 (m_b 4.9) and 1225 UT (m_b 5.2) on March 10, the aftershock area expanded to into a region to the south and beneath the mainshock moment release. All seven well-located aftershocks over the next five days were located in this region, near three of the four foreshocks. This sequence shows that the outlying aftershocks to the south, which clearly extended beyond both the mainshock rupture zone and the seismically active slab as defined by existing seismicity, are related to the spatial expansion of the aftershock zone. Finally, after a short hiatus in activity, a final late stage of aftershock occurrence commenced on March 24 and extended until at least April 20. The aftershocks were scattered throughout the entire aftershock zone, but the most northerly well-located events along the fault plane occurred during this time on March 27 (1120 UT) and April 2 (1318 UT).

These results show that the aftershock area of the 1994 Tonga event expanded by about a factor of two between the early stage (the first 10 hours) when aftershocks were confined to regions near the actual mainshock slip zone, and later stages of aftershock activity. This is similar to average aftershock expansion ratios of shallow earthquakes [*Tajima and Kanamori*, 1985] and demonstrates another similarity between this deep aftershock sequence and typical shallow aftershock sequences.

3.3. Aftershocks Outside the Slab?

Figure 9 shows the positions of the March 9 sequence relative to the 1980-1995 background Tonga slab seismicity. The mainshock hypocenter initiated immediately northward of a narrow, intense region of seismicity that marks the southwestern edge of this near-vertical section of the Tonga slab. The main rupture zone and the early aftershock zone occur within a region of more sparse seismicity in the center and towards the northeast edge of the slab.

Several aftershocks occurred outside the seismically active slab as defined by the 1980-1995 seismicity [*Wiens et al.*, 1994]. An aftershock on March 10 (1414 UT, m_b=4.4) occurred ~15 km beyond the southwestern extent of the background seismicity (Figure 9). This event occurred in a region where little or no rupture occurred during the mainshock [*McGuire et al.*, 1997] but which was actively involved in the intermediate stage of aftershock activity, associated with aftershock expansion toward the south into regions where no aftershocks were found during the first few hours. Two other well located late aftershocks, on March 27 (1120 UT, m_b=5.1) and April 2 (1318 UT, m_b=4.7) occurred ~15 km outside the zone of background seismicity to the northeast. These aftershocks are located in the region near the termination point of the mainshock rupture. Although both well-located aftershocks occurred late in the sequence, several other early aftershocks, such as events 9 and 45 (Table 1), are also found in this region, suggesting this may not be a case of late aftershock expansion. The three outlying aftershocks are extremely well located, with relative location uncertainties of 3-6 kilometers. Tables 5a and 5b list the arrivals used for two of the events, along with the relative residuals.

The location of aftershocks outside the region of background seismicity suggests that transient processes that

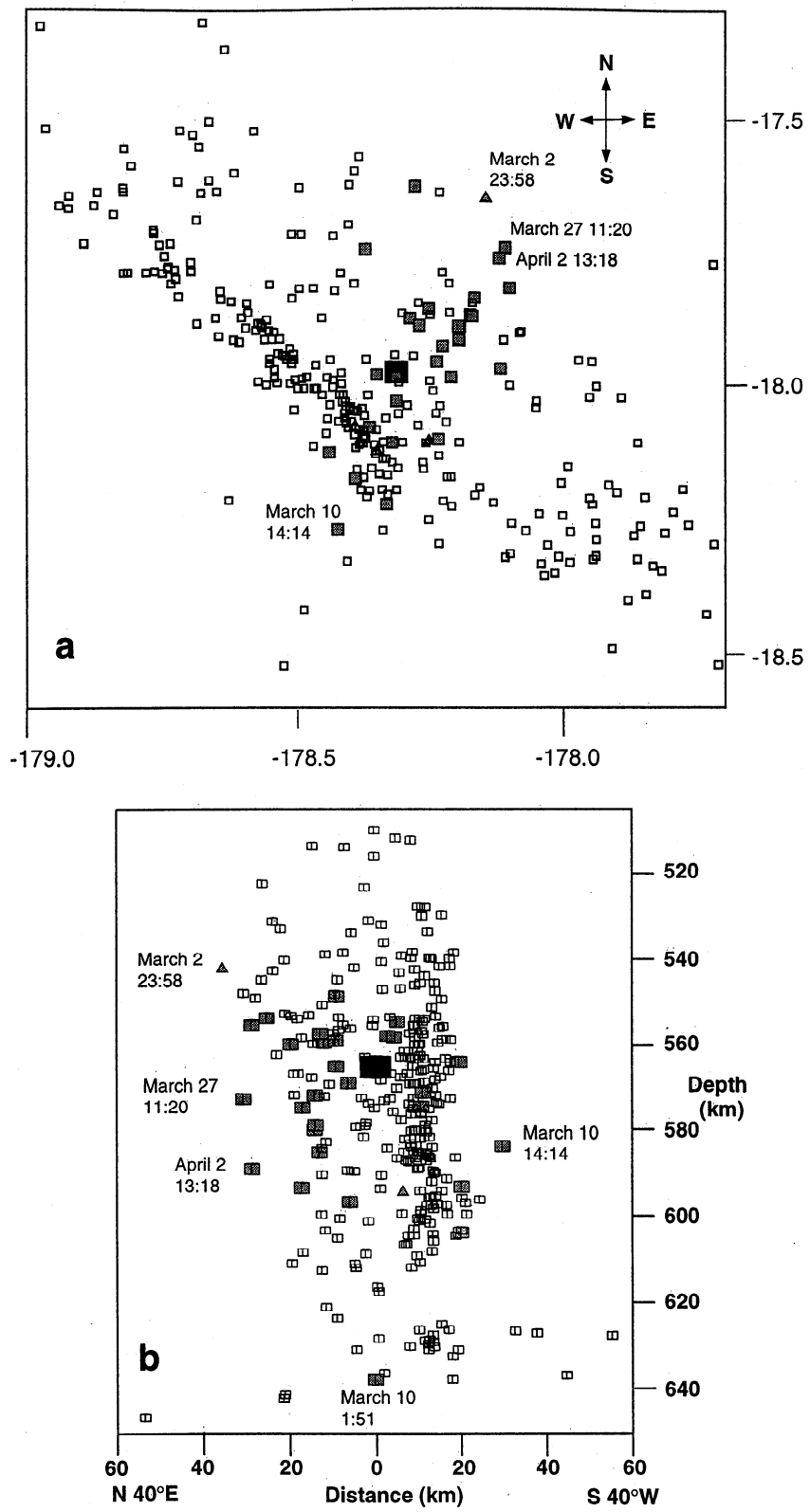

Figure 9. The March 9, 1994, Tonga deep earthquake sequence along with background slab seismicity from 1980 to 1995. The mainshock is represented by the large solid square, aftershocks by shaded squares, foreshocks by shaded triangles, and background seismicity by open symbols. (a) Top view, and (b) view looking edge-on to the northern Tonga slab (from N50°W).

exist immediately following a large deep earthquake permit aftershocks in regions that are too hot for background seismicity. These transient processes may include stress loading beyond the ends of the active rupture, as may be the case for the southern aftershock (March 10, 1414 UT). The northern aftershocks (March 27 and April 2), which are located along the active rupture zone, may also result from thermal perturbations that may accompany active rupture.

Table 5a. Arrival Times Used in Locating the March 10 (1414 UT) Outlying Aftershock

Station code	Phase	Distance, deg	Azimuth, deg	Data Importance	Relative Residuals
LKBA	P	0.44	281	0.1340	-0.35
LBSA	P	2.89	314	0.4504	0.06
LBSA	S	2.89	314	0.2198	0.47
VUN	P	3.03	275	0.0283	-0.13
LTKA	P	4.05	278	0.1931	0.01
NUKU	P	4.12	134	0.3041	0.10
NUKU	S	4.12	134	0.2055	-0.19
VAVA	P	4.18	95	0.2014	0.22
VAVA	S	4.18	95	0.0389	-0.11
EUAT	P	4.40	134	0.1486	0.16
EUAT	S	4.40	134	0.2111	-0.48
AFI	P	7.70	56	0.2216	-0.19
DZM	P	14.74	253	0.0355	0.83
ARMA	P	29.77	240	0.0343	0.19
CNB	P	33.21	233	0.0386	0.35
CTAO	P	33.42	261	0.2942	0.16
PMG	P	34.57	280	0.1430	-1.02
SB01	P	39.54	252	0.3291	0.08
WB2	P	44.59	260	0.0256	0.09
ASPA	P	44.72	255	0.0271	0.13
SRU	P	85.27	46	0.0609	-0.11
FBA	P	86.20	13	0.0850	0.85
PV09	P	85.95	47	0.0776	-0.12
LTX	P	86.18	58	0.0788	0.47
PV08	P	86.32	47	0.0734	-0.23
ALQ	P	86.32	51	0.0733	0.39
YKA	P	94.69	25	0.0936	-0.42

3.4. Aftershock Focal Mechanisms and the Tectonics of the Tonga Slab

The dense region of seismicity around the March 9 earthquake shows a diversity of faulting types, with the dip-slip mechanism of the mainshock one of several common focal mechanisms [*Giardini and Lundgren*, 1995]. Most of the aftershocks, including March 10 (0346, 1225, and 1908 UT), March 24 (1717 UT), March 27 (1120 UT) and April 20 (2335 UT) show slightly oblique dip-slip faulting along fault planes trending NE. The more steeply dipping nodal plane of these events is similar to the presumed fault plane of the main shock, and these focal mechanisms are quite similar to the initial subevent of the mainshock, except they show a smaller strike-slip component. The outlying aftershock to the north (March 27) shows a nodal plane strike (16°) that is more northerly than the first subevent of the mainshock (strike 25°) as well as most of the aftershocks (Figure 10). This orientation, however, is similar to the second subevent of the mainshock (strike 5°) which occurred in the same region. The March 25 aftershock, ~25 km west of the northern end of the rupture, also shows a north-south striking vertical fault plane similar to the last subevent of the mainshock. These aftershock mechanisms are consistent with the rotation of the mainshock fault plane as the rupture progressed toward the north [*McGuire et al.*, 1997].

The March 9 (2350 UT) and 0151 and 1029 UT aftershocks on March 10 show focal mechanisms that are significantly different from the mainshock and most of the aftershocks, although they are similar to other centroid moment tensor (CMT) solutions in this region. The 0151 UT aftershock was a triggered event at the bottom of the active seismic zone about 70 km below the mainshock. It shows a focal mechanism similar to the CMT solutions of several other earthquakes at depths below 610 km in this region. The March 10 (1029 UT) event shows a strike-slip mechanism that is clearly different than the mainshock and most of the aftershocks, as demonstrated by the different first motions observed at regional stations (Figures 6 and 7). This event occurred at the intersection of the mainshock fault plane and a very active, vertical northwest-striking seismicity lineament (Figures 9 and 10). The earthquakes along this lineament are characterized by left-lateral strike-slip motion along a northwest trending nodal plane, which is consistent with the focal mechanism of the 1029 UT aftershock (Figure 7). The different focal mechanisms of the aftershocks reflect the complexity of the faulting in this region, as is also indicated by the variability of CMT solutions [*Giardini*, 1992].

Despite some variability, all the aftershock focal mechanisms are characterized by compressional axes dipping towards the west. Figure 11 compares the compressional (*P*) and tensional (*T*) axes of the mainshock sub-events,

Table 5b. Arrival Times Used in Locating the March 27 (11:20) Outlying Aftershock

Station Code	Phase	Distance, deg	Azimuth, deg	Data Importance	Relative Residuals
LKBA	P	0.86	239	0.1910	0.25
LKBA	S	0.86	239	0.0235	0.10
LBSA	P	2.82	301	0.2721	0.05
LBSA	S	2.82	301	0.1667	-0.27
VUN	P	3.34	266	0.0153	0.33
SUVA	P	3.35	264	0.1190	-0.13
SUVA	S	3.35	264	0.0326	-0.52
VAVA	P	3.96	103	0.1666	0.57
VAVA	S	3.96	103	0.1388	-1.03
NUKU	P	4.31	142	0.0551	0.03
NUKU	S	4.31	142	0.2322	-0.61
LTKA	P	4.32	271	0.2271	0.12
LTKA	S	4.32	271	0.0336	0.54
EUAT	P	4.58	141	0.1500	-0.08
EUAT	S	4.58	141	0.0657	-0.42
NIUE	P	7.84	100	0.0388	0.28
NIUE	S	7.84	100	0.0845	-0.92
DZM	P	15.20	251	0.0192	-0.44
KUZ	P	19.68	195	0.0253	0.24
WLZ	P	20.77	194	0.0211	0.20
MNG	P	23.43	192	0.0237	0.63
QRZ	P	24.36	198	0.0225	-0.53
THZ	P	25.13	196	0.0249	0.57
KHZ	P	25.58	195	0.0220	0.06
LTZ	P	26.25	196	0.0244	0.15
WVZ	P	26.95	198	0.0228	-0.09
MQZ	P	27.01	195	0.0176	0.15
AFR	P	26.92	94	0.0343	0.06
PAE	P	27.10	94	0.0341	0.13
PPT	P	27.11	94	0.0342	0.12
EWZ	P	27.31	198	0.0246	-0.10
PPN	P	27.25	94	0.0342	0.11
TVO	P	27.40	94	0.0340	-0.23
LMZ	P	27.99	200	0.0241	0.03

An additional 53 *P* arrivals at distances of 28-94° were also used; arrivals from stations SVA, WCZ, MAT, BDT, and CHTO were deleted due to large residuals.

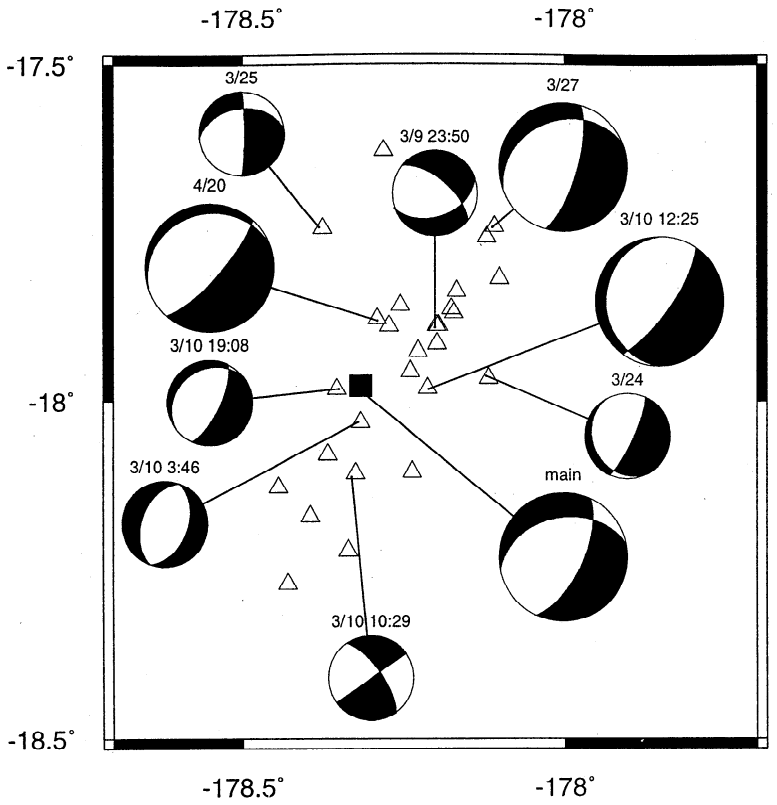

Figure 10. Focal mechanisms of aftershocks plotted on a map view of the aftershock seismicity. The *P* wave focal mechanisms are plotted as lower hemisphere projections, with compressional quadrants filled in. Larger focal mechanisms represent solutions determined by waveform inversion, which has smaller uncertainties.

aftershocks, and background seismicity. The *P* and *T* axes of the March 9 mainshock and aftershocks are similar to the stress axes shown by the background seismicity. The most consistent feature of the data set as a whole is *P* axes dipping toward the west. This is compatible with previous analyses of the stress state of this region, which suggest intense shortening in the deep Tonga slab [*Giardini and Woodhouse*, 1984; *Nothard et al.*, 1996]. In the region of the 1994 earthquake the compression also includes a component along the strike of the slab.

3.5. Implications for the Mechanism of Deep Earthquakes

Various models have been proposed to explain the existence of earthquakes to depths of nearly 700 km. The

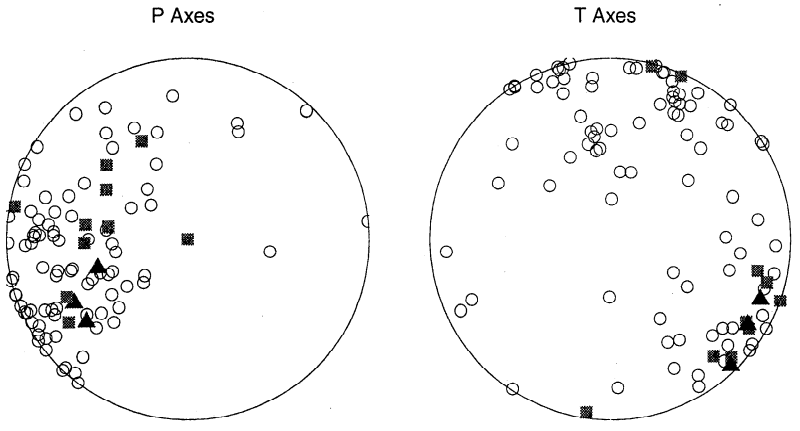

Figure 11. Compressional (*P*) and tensional (*T*) axes of the mainshock subevents (triangles), aftershocks (squares), and all Harvard CMT solutions from the region shown in Figure 9 (circles). The *P* and *T* axes of the mainshock and aftershocks are similar to those of the background seismicity, which show a large scatter, but generally show *P* axes dipping westward and down.

most popular mechanisms include transformational faulting [*Kirby*, 1987, *Green and Birnley*, 1989; *Green and Houston*, 1995; *Kirby et al.*, 1996], dehydration reactions or fluid assisted slip on pre-existing faults [*Meade and Jeanloz*, 1991; *Silver et al.*, 1995], ductile shear failure [*Hobbs and Ord*, 1988; *Ogawa*, 1987], and melting [*Kanamori et al.*, 1998].

The low occurrence rate of aftershocks has often been cited as a difference between shallow and deep earthquakes, implying a very different mechanism for deep earthquakes. The results of this study show that the most prolific deep earthquake aftershock sequence shows considerable similarities to shallow earthquakes. By most statistical measures, such as aftershock productivity, magnitude-frequency relation, temporal decay pattern, and aftershock expansion rate, this sequence is indistinguishable from a rather weak shallow aftershock sequence. This implies that the processes generating the deep aftershocks of the 1994 Tonga event must have at least a superficial similarity to processes involved in shallow sequences.

It is not clear whether very different physical processes might still produce similar statistical behavior. For example, relatively simple physical models can give rise to the most commonly observed statistical quantities, such as temporal decay and aftershock expansion patterns [*Dieterich*, 1994] and magnitude-frequency relations [*Rundle*, 1989]. Failure phenomenon other than brittle failure may be largely governed by similar laws and thus show similar statistical behavior. It should also be noted that although this aftershock sequence showed many similarities with shallow sequences, most deep earthquake sequences are much weaker, and the general dependence of aftershock productivity and deep earthquake *b* values on slab thermal structure is not explained [*Wiens and Gilbert*, 1996].

The existence of aftershocks outside the limits of the normal Wadati-Benioff zone and the overall width of the aftershock zone are problematic for the transformational faulting hypothesis [*Green and Houston*, 1995; *Kirby et al.*, 1996]. In this model, all deep earthquakes should be associated with the olivine to β or γ phase transformation within a narrow metastable olivine wedge. Since the limits of the background seismicity presumably reflect the width of the metastable wedge in this model, it is difficult to understand how aftershocks as well as mainshock rupture could occur outside this region. The transformational faulting model is also incompatible with the overall width of the aftershock zone, which is ~ 70 km. Mineralogical models of the Tonga slab based on thermal modeling, thermodynamic data, and the kinetics of the olivine to β phase reaction [*Rubie and Ross*, 1994] suggest that the metastable wedge should be of the order of 15-30 km wide [*Koper et al.*, 1998], considerably less than the total aftershock zone width of 65 km. Much larger volumes of metastable material are precluded, since they would generate excessive buoyancy forces that would prevent the further descent of the slab.

The observations described here are more compatible with the ductile shear instability or fault melting models for deep earthquakes. In these models, deep earthquake faulting would be a temperature-controlled phenomenon, thus explaining the dependence of aftershock productivity on slab temperature [*Wiens and Gilbert*, 1996]. Large earthquake ruptures, once nucleated, could readily propagate outside the Wadati-Benioff zone defined by the smaller earthquakes into material that is normally too hot to undergo sudden shear failure [*McGuire et al.*, 1997], and aftershocks could nucleate in this region due to transient thermal and mechanical phenomena associated with the larger mainshock rupture.

4. Conclusions

The aftershock sequence of the March 9, 1994 Tonga earthquake is the strongest known aftershock sequence of a deep earthquake. By most statistical measures this sequence is indistinguishable from a weak shallow aftershock sequence. The rupture velocity (as a percent of the shear velocity) and static stress drop are also quite similar to shallow earthquakes [*McGuire et al.*, 1997; *Tibi et al.*, 1999]. These observations suggest that the processes generating the rupture and the aftershock sequence of the 1994 Tonga earthquake have some similarity to processes involved in shallow sequences. The 1994 Tonga earthquake may be relatively typical of large deep earthquakes in cold slabs, which show rupture velocities, stress drops, and aftershock sequences that are similar to shallow earthquakes.

The March 9 sequence offers important insight into the relationship between deep earthquake aftershocks and rupture. Aftershocks in the initial 10 hours were located near regions of large slip during the mainshock, whereas later aftershocks expanded into regions with little or no slip. Most of the aftershocks show focal mechanisms similar to the mainshock, and indicating strong compression in the vertical and along-strike directions. Several aftershocks are located outside the bounds of normal Wadati-Benioff zone seismicity in this region, suggesting that transient processes associated with the mainshock rupture allowed them to occur at temperatures higher than typically bound seismicity in this region. This observation is difficult to reconcile with the transformational faulting hypothesis for deep earthquakes, which would generally suggest that deep earthquakes and aftershocks should only occur within a narrow metastable olivine wedge.

Acknowledgments. We thank Patrick Shore (Washington University), Paul Friberg (Lamont PASSCAL Instrument Center), Mike Bevis (University of Hawaii), George Hade (Cornell), Kiti Draunidalo (Fiji Mineral Resources Department), Simone Helu (Tonga Ministry of Lands), and George Sionihalo (Niue Department of Survey) for assistance in deploying the seismographs. We also thank Hersh Gilbert, Erich Roth, and Brian Park-Li for assistance in processing the data. Some aftershock waveforms from the SKIPPY array were provided by Rob van der Hilst. Instruments for this study were obtained from the PASSCAL program of IRIS (Incorporated Research Institutions in Seismology), and teleseismic data were obtained from the IRIS Data Management Center. This research was supported by the National Science Foundation under grants EAR 9219675, EAR9418942, and EAR9805309.

References

Davis, S.D., and C. Frohlich, Single-link cluster analysis of earthquake aftershocks: Decay laws and regional variations, *J. Geophys. Res.*, *96*, 6335-6350, 1991.

Dieterich, J., A constitutive law for rate of earthquake production and its application to earthquake clustering, *J. Geophys. Res.*, *99*, 2601-2618, 1994.

Dreger, D., The large aftershocks of the Northridge earthquake and their relationship to mainshock slip and fault-zone complexity, *Bull. Seismol. Soc. Am.*, *87*, 1259-1266, 1997.

Dziewonski, A. M., T.-A. Chou, and J. H. Woodhouse, Determination of earthquake source parameters from waveform data for studies of global and regional seismicity, J. Geophys. Res., 86, 2825-2852, 1981.

Frohlich, C., Aftershocks and temporal clustering of deep earthquakes, *J. Geophys. Res.*, *92*, 13,944-13,956, 1987.

Frohlich, C., The nature of deep-focus earthquakes, *Annu. Rev. Earth Planet. Sci.*, *17*, 227-254, 1989.

Frohlich, C., and S.D. Davis, Teleseismic b values: Or, much ado about 1.0, *J. Geophys. Res.*, *98*, 631-644, 1993.

Giardini, D., Space-time distribution of deep seismic deformation in Tonga, *Phys. Earth Planet. Inter.*, *74*, 75-88, 1992.

Giardini, D., and P. Lundgren, The June 9 Bolivia and March 9 Fiji deep earthquakes of 1994: Geodynamic implications, *Geophys. Res. Lett.*, *22*, 2281-2284, 1995.

Giardini, D., and J.H. Woodhouse, Deep seismicity and modes of deformation in Tonga subduction zone, *Nature*, *307*, 505-509, 1984.

Goes, S., and J. Ritsema, A broadband *P* wave analysis of the large deep Fiji Island and Bolivia earthquakes of 1994, *Geophys. Res. Lett.*, *22*, 2249-2252, 1995.

Gomberg, J., M.L. Blanpied, and N.M. Beeler, Transient triggering of near and distant earthquakes, *Bull. Seismol. Soc. Am.*, *87*, 294-309, 1997.

Green, H. W. I., and P. C. Birnley, A new self-organizing mechanism for deep focus earthquakes, *Nature, 341,* 733-737, 1989.

Green, H.W.I., and H. Houston, The mechanics of deep earthquakes, *Annu. Rev. Earth Planet Sci.*, *24*, 169-213, 1995.

Hill, D. P., et al., Seismicity remotely triggered by the magnitude 7.3 Landers, California earthquake, *Science, 260,* 1617-1623, 1993.

Hobbs, B.E., and A. Ord, Plastic instabilities: Implications for the origin of intermediate and deep focus earthquakes, *J. Geophys. Res.*, *93*, 10,521-10,540, 1988.

Jordan, T.H., and K.A. Sverdrup, Teleseismic location techniques and their application to earthquake clusters in the South-Central Pacific, *Bull. Seismol. Soc. Am.*, *71*, 1105-1130, 1981.

Kanamori, H., D.L. Anderson, and T.H. Heaton, Frictional melting during faulting, *Science*, *279*, 839, 1998.

Kennett, B.L.N., *Seismic wave propagation in stratified media*, 339 pp., Cambridge Univ. Press, New York, 1983.

King, G.C.P., R.S. Stein, and J. Lin, Static stress changes and the triggering of earthquakes, *Bull. Seismol. Soc. Am.*, *84*, 935-953, 1994.

Kirby, S.H., Localized polymorphic phase transformations in high-pressure faults and applications to the physical mechanism of deep earthquakes, *J. Geophys. Res.*, *92*, 13,789-13,800, 1987.

Kirby, S.H., S. Stein, E.A. Okal, and D. Rubie, Deep earthquakes and metastable mantle phase transformations in subducting oceanic lithosphere, *Rev. Geophys.*, *34*, 261-306, 1996.

Kisslinger, C., Aftershocks and fault-zone properties, *Adv. Geophys.*, *38*, 1-36, 1996.

Kisslinger, C., and A. Hasegawa, Seismotectonics of intermediate-depth earthquakes from properties of aftershock sequences, *Tectonophysics*, *197*, 27-40, 1991.

Kisslinger, C., and L.M. Jones, Properties of aftershock sequences in Southern California, *J. Geophys. Res.*, *96*, 11,947-11,958, 1991.

Koper, K.D., D.A. Wiens, L.M. Dorman, J.A. Hildebrand, and S.C. Webb, Modeling the Tonga slab: Can travel time data resolve a metastable olivine wedge?, *J. Geophys. Res.*, *103*, 30,079-30,100, 1998.

Langston, C.A., and D.V. Helmberger, A procedure for modelling shallow dislocation sources, *Geophys. J. R. Astron. Soc.*, *42*, 117-130, 1975.

Lundgren, P., and D. Giardini, The June 9 Bolivia and March 9 Fiji deep earthquakes of 1994: I. Source processes, *Geophys. Res. Lett.*, *22*, 2241-2244, 1995.

McGuire, J.J., D.A. Wiens, P.J. Shore, and M.G. Bevis, The March 9, 1994 deep Tonga earthquake: Rupture outside the seismically active slab, *J. Geophys. Res.*, *102*, 15,163-15,182, 1997.

Meade, C., and R. Jeanloz, Deep-focus earthquakes and recyling of water into the Earth's mantle, *Science*, *252*, 68-72, 1991.

Mendoza, C., and S. Hartzell, Aftershock patterns and mainshock faulting, *Bull. Seismol. Soc. Am.*, *79*, 655-669, 1988.

Mikumo, T., and T. Miyatake, Earthquake sequences on a frictional fault model with non-uniform frictions and near-field seismic waves, *Geophys. J. R. Astron. Soc.*, *59*, 497-522, 1979.

Myers, S.C., T.C. Wallace, S.L. Beck, P.G. Silver, G. Zandt, J. Vandecar, and E. Minaya, Implications of spatial and temporal development of the aftershock sequence for the Mw 8.3 June 9, 1994 deep Bolivian earthquake, *Geophys. Res. Lett.*, *22*, 2269-2272, 1995.

Nothard, S., J. Haines, J. Jackson, and B. Holt, Distributed deformation in the subducting lithosphere, *Geophys. J. Int.*, *127*, 328-338, 1996.

Nyffenegger, P., and C. Frohlich, Aftershock occurrence rate decay properties for intermediate and deep earthquake sequences, *Geophys. Res. Lett., 27,* 1221-1224, 2000.

Ogata, Y., Estimation of the parameters in the modified Omori formula for aftershock frequencies by the maximum likelihood procedure, *J. Phys. Earth*, *31*, 115-124, 1983.

Ogawa, M., Shear instability in a visco-elastic material as the cause of deep focus earthquakes, *J. Geophys. Res.*, *92*, 13,801-13,810, 1987.

Okal, E. A., A reassessment of the deep Fiji earthquake of 26 May 1932, *Tectonophysics, 275*, 313-330, 1997.

Okal, E. A., and B. A. Romanowicz, On the variation of b-values with earthquake size, *Phys. Earth Planet. Inter., 87,* 55-76, 1994.

Page, R., Focal depths of aftershocks, *J. Geophys. Res.*, *73*, 3897-3903, 1968.

Pavlis, G.L., and M.W. Hamburger, Aftershock sequences of intermediate-depth earthquakes in the Pamir-Hindu Kush seismic zone, *J. Geophys. Res.*, *96*, 18107-18117, 1991.

Rubie, D.C., and C.R. Ross II, Kinetics of the olivine-spinel transformation in subducting lithosphere: Experimental constraints and implications for deep slab processes, *Phys. Earth Planet Inter.*, *86*, 223-241, 1994.

Rundle, J.B., Derivation of the complete Gutenberg-Richter magnitude-frequency relation using the principle of scale invariance, *J. Geophys. Res.*, *94*, 12,337-12,342, 1989.

Silver, P., S. Beck, T. Wallace, C. Meade, S. Myers, D. James, and R. Kuehnel, Rupture characteristics of the deep Bolivian earthquake of 9 June 1994 and the mechanism of deep-focus earthquakes, *Science*, *268*, 69-73, 1995.

Tajima, F., and H. Kanamori, Global survey of aftershock area expansion patterns, *Phys. Earth Planet. Inter.*, *40*, 77-134, 1985.

Tibi, R., C.H. Estabrook, and G. Bock, The 1996 June 17 Flores Sea and 1994 March 9 Tonga-Fiji earthquakes: source processes and deep earthquake mechanisms, *Geophys. J. Int.*, *138*, 625-642, 1999.

Utsu, T., A statistical study on the occurrence of aftershocks, *Geophys. Mag.*, *30*, 521-605, 1961.

Wiens, D.A., and H.J. Gilbert, Effect of slab temperature on deep-earthquake aftershock productivity and magnitude-frequency relations, *Nature*, *384*, 153-156, 1996.

Wiens, D.A., J.J. McGuire, P.J. Shore, M.G. Bevis, K. Draunidalo, G. Prasad, and S. Helu, A deep earthquake aftershock sequence and implications for the rupture mechanism of deep earthquakes, *Nature*, *372*, 540-543, 1994.

Wiens, D.A., H.J. Gilbert, B. Hicks, M.E. Wysession, and P.J. Shore, Aftershock sequences of moderate-sized intermediate and deep earthquakes in the Tonga subduction zone, *Geophys. Res. Lett.*, *24*, 2059-2062, 1997.

Wu, L –R., and W.-P. Chen, Anomalous aftershocks of deep earthquakes in Mariana, *Geophys. Res. Lett., 26,* 1977-1980, 1999

Willemann, R.J., and C. Frohlich, Spatial patterns of aftershocks of deep focus earthquakes, *J. Geophys. Res.*, *92*, 13927-13943, 1987.

J. J. McGuiire, Department of Earth, Atmospheric, and Planetary Sciences, MIT, Cambridge, MA 20139 (jeff@quake.mit.edu)

D. A. Wiens, Department of Earth and Planetary Sciences, Washington University, One Brookings Dr., St. Louis, MO 63130 (doug@seismo.wustl.edu)

(Received October 25, 1999; revised March 7, 2000; accepted March 16, 2000)